Journal of Photochemistry and Photobiology A: Chemistry 332 (2017) 391–398

Contents lists available at ScienceDirect

Journal of Photochemistry and Photobiology A: Chemistry

journal homepage: www.elsevier.com/locate/jphotochem

Full Length Article

Enhanced charge separation through modulation of defect-state in wide band-gap semiconductor for potential photocatalysis application: Ultrafast spectroscopy and computational studies

Tuhin Kumar Maji[a], Damayanti Bagchi[a], Prasenjit Kar[a], Debjani Karmakar[b,*], Samir Kumar Pal[a,*]

[a] Department of Chemical, Biological and Macromolecular Sciences, S. N. Bose National Centre for Basic Sciences, Block JD, Sector III, SaltLake, Kolkata 700 106, India

[b] Technical Physics Division, Bhaba Atomic Research Centre, Mumbai 400085, India

ARTICLE INFO

Article history:
Received 9 August 2016
Received in revised form 2 September 2016
Accepted 16 September 2016
Available online 20 September 2016

Keywords:
Chloride attached ZnO NPs
Photocatalysis
Trap state and DFT

ABSTRACT

Structural defects of wide band gap semiconductors play important role in their functionality. Defect mediated recombination of photoinduced electron-hole pair in the semiconductors for their photocatalytic activities, is detrimental. In the case of ZnO nanostructures, radiative recombination upon band-gap photo-excitation (3.37 eV) originated from different surface defects (mainly Oxygen vacancies at 2.50 eV (V^{+}) and 2.25 eV (V^{++}) with respect to valance and conduction bands respectively) of crystal lattice, acquires immense interest for both fundamental scientific point of view and for the betterment of their manifold applications. The present work indicates that for transition metal semiconducting oxides, use of anionic attachment like Cl^{-} as surface defect healer proves to be more useful for photocatalytic application than bulk doping using cationic dopant like Mn. ZnO NPs of different sizes (5 nm and 30 nm) are synthesized via precipitation method and allowed to interact with chloride ions in aqueous solution. A variety of electron microscopy and picosecond resolved spectroscopic techniques have been employed to study the role of chloride ions for the enhanced photoinduced charge separation in the aqueous environments. Our first principles density-functional calculations for ZnO nanoclusters with surface oxygen vacancy indicate introduction of trap states within the band gap of the nanoclusters. These states effectively confine the photoinduced electrons and thus essentially reduce the photocatalytic yield with respect to pristine ZnO. However, upon Cl^{-} attachment to the defect states, the energy of the trap states were found to be healed, recovering the efficacy of reactive oxygen species (ROS) generation in the aqueous solution. We have also impregnated Mn^{2+} ions to the ZnO lattice using precipitation method in solution phase. The DFT calculation on the Mn^{2+} ion impregnated ZnO lattice reveals more defect states compare to that of pristine lattice. The rate of electron recombination is found to be much faster through non-radiative pathway (ground state recovery), leading to a decrease in photocatalytic activity in the case of Mn-doped ZnO. Attachment of Cl^{-} to the Mn-doped ZnO partially recovers the ROS generation, which is consistent with healing of deep trap states. The present work is anticipated to provide a new insight into the surface defect modulation of ZnO in potential photocatalysis application.

1. Introduction

With increasing concern over the depletion in the quality of drinking water, contaminants from industrial waste as hazardous pollutants, is one of the greatest issues that humanity will be facing in upcoming years [1,2]. The conventional waste water treating techniques as chlorination, ozonation etc. are less suitable in view of large scale applications due to high cost and many other speculative side effects [3]. In this aspect, heterogeneous photocatalysis based on nanostructured semiconductors is an environment-friendly alternative approach [4,5]. Degradation of the organic pollutants by electron-hole pair, generated due to

* Corresponding authors.
E-mail addresses: debjan@barc.gov.in (D. Karmakar), skpal@bose.res.in (S.K. Pal).

http://dx.doi.org/10.1016/j.jphotochem.2016.09.017
1010-6030/

photo-excitation of the semiconductor catalyst, is the key point towards the development of effective low-cost materials for waste water management [4]. More than 44 years after the pioneering work of Fujishima and Honda [6], the search for suitable semiconductors to be employed for dissociation of organic pollutants into less toxic products is still an open challenge [7].

Out of many different photocatalysts, ZnO and TiO_2 have been extensively studied [8] because of their strong oxidizing abilities for the decomposition of organic pollutants [9], chemical stability, non-toxicity, abundance in nature, environmental friendliness and low-cost [10,11]. In fact ZnO and TiO_2 exhibit similar band-gap energy and anticipated to show nearly same photocatalytic activities [12]. However, presence of several bulk and surface defects in ZnO limits its use for various applications over TiO_2. So the modulation of defect state can be used as a tool to tune up the photocatalysis and other applications of ZnO over TiO_2. For ZnO nanostructures, a rich variety of defect chemistry is known to be present, *viz.* zinc vacancy (V_{Zn}), oxygen vacancy (V_O), zinc interstitial (Zn_i), oxygen interstitial (O_i), or antisite oxygen (O_{Zn}) [13]. Whereas, selective native defects with controlled defect density are beneficial for photocatalytic activity of ZnO nanostructures, higher defect densities are known to reveal inverse effects [14]. Common defects like V_O existing in the ZnO crystal generally worsen the photocatalytic activity of ZnO. It is therefore significantly important to find an effective method to heal these defects [15]. The defect state modulation of ZnO by cationic dopants like Mn (II), Co (II), Fe (II) etc., anionic dopants like N_2 or attachment of ad-atoms shows significant structural perturbation leading to different catalytic properties [16,17]. Sometime structurally modified ZnO demonstrate an improved photocatalysis even compared to commercialized TiO_2 nanostructures [18].

In the present study, we have synthesized ZnO nanoparticles (NPs) of various sizes in the pristine form and with cationic dopant and anionic healer like Mn^{2+} and chloride ions respectively. These systems are structurally characterized using high resolution electron microcopy (HRTEM, FEG-SEM), EDAX and X-ray diffraction techniques. A detailed UV–vis and fluorescence spectroscopy followed by picosecond resolved time correlated single photon counting (TCSPC) have been utilized to characterize the absorption and emission properties of the defect states and their healing mechanism upon introduction of chloride ions in aqueous solution. The manifestation of the modulation of the defect states in the NPs for their photocatalytic activity through ROS generation has also been explored. First principles theoretical calculations are performed on similarly constructed nanostructures to understand the appearance and absence of defect modulated energy levels. Our studies imply that modulation of the defect states is very crucial for the application of the NPs in photocatalysis.

2. Experimental section

2.1. Reagents

Sodium carbonate (Na_2CO_3) Potassium Chloride (KCl) and sodium hydroxide (NaOH) from Merck, Zinc acetate dehydrate ($(CH_3COO)_2Zn$, $2H_2O$) from Sigma Aldrich, Polyethylene glycol PEG ($M_w = 1000$) from Fluka, Manganese (II) Chloride tetrahydrate ($MnCl_2$, $4H_2O$) from Loba Chemie are used for synthesis. All chemicals employed were of analytical grade and used without further purification.

2.2. Synthesis of ZnO-NPs

ZnO NPs of size ~5 nm was prepared in ethanolic medium following method as described in reference [19]. 20 mL 4 mM zinc acetate dihydrate, $(CH_3COO)_2Zn$, $2H_2O$ was heated at 60 °C around 30 min. 20 mL 4 mM sodium hydroxide solution in ethanol was added with it. The mixture was vigorously stirred for 2 h at 60 °C. The resulting solution was cooled at room temperature and stored at 4 °C until further use. ZnO NPs of size ~30 nm was synthesized by the precipitation method [20]. Firstly, PEG (10% V/V) was taken in a three naked flask. Next, 0.05 M zinc acetate and 0.1 M Na_2CO_3 was added simultaneously into the PEG solution. The system was stirred vigorously for 2 h. Then the precipitate was washed with double distilled water, ammonia solution (pH = 9) and ethanol. It was dried at room temperature. The precipitate was calcined in muffle furnace at 450 °C for 3 h. Finally ZnO NP of size ~ 25–30 nm were prepared.

2.3. Preparation of chloride attached ZnO and Mn-doped ZnO

5 mg ZnO NP (size ~30 nm) was taken in 10 mL distilled water. 1 mL 0.1 M KCl solution was mixed in the solution at room temperature and magnetically stirred for 12 h to obtain chloride attached ZnO NP. It is then dried and dispersed in water for further studies. For Mn-doped ZnO, 5 mM $MnCl_2$ solution was added to the reaction mixture containing zinc acetate following the same procedure of synthesis as 30 nm NP.

2.4. Characterization methods

Surface morphology of the NPs was confirmed using Field Emission Scanning Electron Microscopy (FESEM, QUANTA FEG 250). The grids for TEM analysis were prepared by applying a drop of diluted solution of the sample on the top of carbon coated TEM grid [21]. The particle size of the samples were determined from micrograph recorded of magnification 100000× using and FEI (Technai S-Twin). X-Ray Diffraction (XRD) pattern were carried out with a PANalytical XPERTPRO diffractometer to characterize the crystal phase. For steady state and time resolved optical study, we have followed the methodology as described in reference [22]. Absorption and emission were monitored using the Shimadzu UV-2430 and Jubin Yvon Fluorolog respectively. Picosecond resolved spectroscopic studies were done using a commercial time correlated single photon counting (TCSPC) setup from Edinburgh Instruments with instrument response function (IRF = 80 ps) upon excitation at 375 nm.

For photocatalysis studies, 1 mg photocatalyst was taken in 2 mL deionized water (DI).Methyl Orange (MO) in DI was used as the test contaminant [23]. The initial concentration of MO was taken 1 mM for all the experiments. Around 500 μL of 1 mM MO solution was added to 2 mL solution to make the initial O.D. 0.6 a.u. @ 461 nm. A homemade UV source (of intensity 300W and wavelength $\lambda \geq 365$ nm) has been used as light source. The mixture of photocatalyst and contaminant was irradiated with UV irradiation and absorbance data were collected with an interval of 10 min. The percentage of degradation (% DE) was determined by the equation –

$$\%DE = \frac{I_0 - I}{I_0} \times 100 \quad (1)$$

where I_0 is the initial absorption intensity of MO at $\lambda_{max} = 461$ nm and I is the absorption intensity after UV irradiation.

3. Computational details

First-principles spin-polarized density functional calculations are performed using Projector augmented wave (PAW) method on a $Zn_{50}O_{50}$ cluster in a cubical box of side ~23 Å. Before structural relaxation, the average size of the cluster was ~1 nm, so as to resemble the order of experimental particle-size.

The exchange-correlation interactions are treated by the generalized gradient approximation (GGA) with Perdew-Burke-Ernzerhof (PBE) exchange functionals using Vienna Ab-initio Simulation package (VASP) [24]. An energy cut-off of 500 eV was used for the plane-wave expansion of PAWs. Keeping in mind the large box-size and the corresponding tiny Brillouin zone, we have employed only single *k*-point (Γ- point) for complete geometry optimization and electronic structure calculations. Van der Waal's interactions are incorporated in this calculation by using DFT-D2 method of Grimme [25], as implemented in VASP [24]. The complete cluster assembly is structurally optimized after permitting relaxation of both lattice parameters and ionic

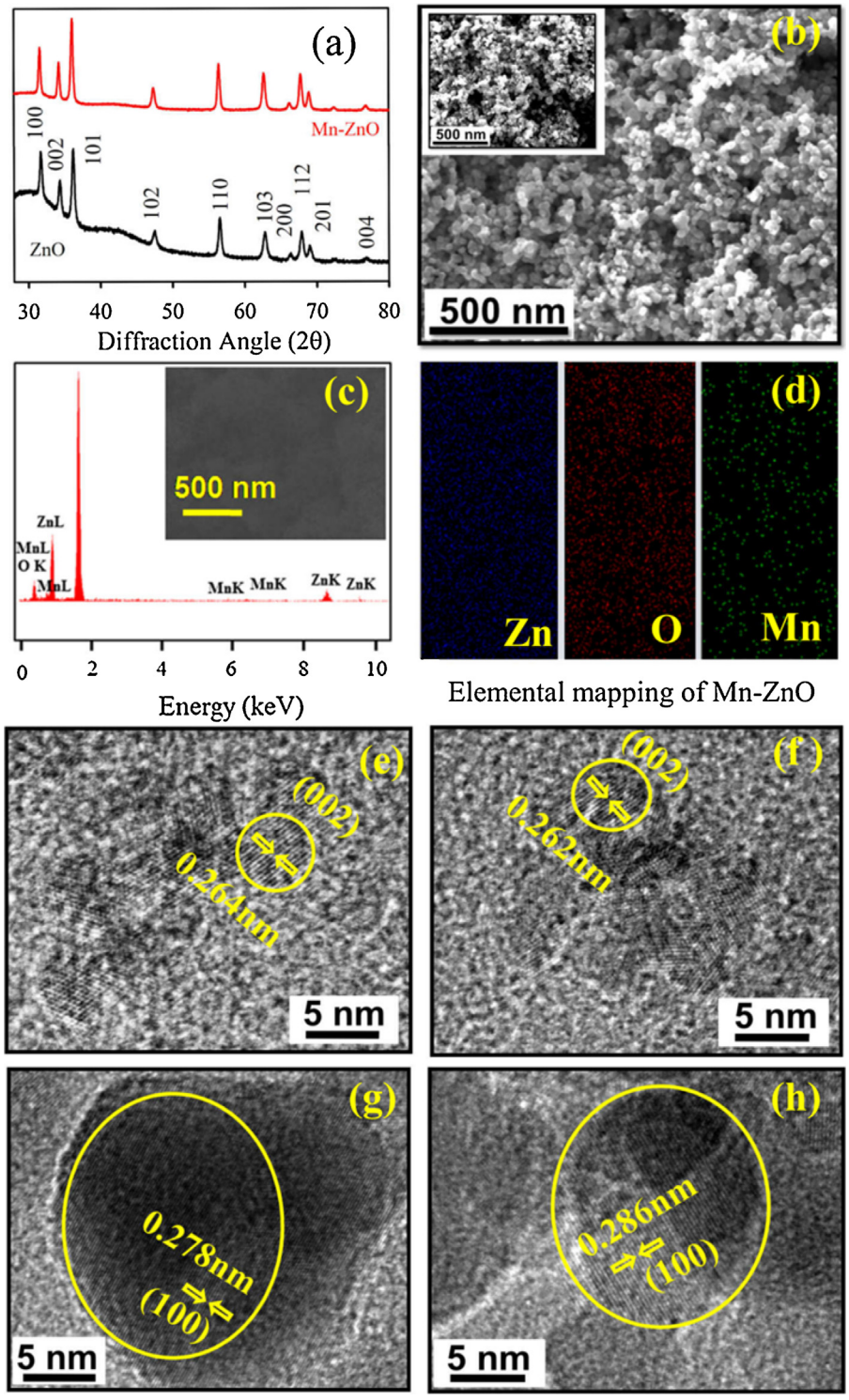

Fig. 1. (a) XRD pattern of ZnO (black) and Mn-doped ZnO (red). (b) FESEM image of 30 nm ZnO NP. Inset shows SEM image of 30 nm Mn-doped ZnO NP, (c) EDAX spectrum of Mn-doped ZnO 30 nm NP. The inset shows the SEM image of the region where EDAX has been scanned. (d) Elemental mapping images of Mn-doped ZnO NP are shown for Zn (blue), O (red) and Mn (green). High Resolution TEM of (e) ZnO (5 nm NP), (f) Mn-doped ZnO (5 nm NP), (g) ZnO (30 nm NP) and (h) Mn-doped ZnO (30 nm NP). (For interpretation of the references to color in this figure legend, the reader is referred to the web version of this article.)

positions following conjugate gradient algorithm [24] until the Hellmann-Feynman forces acting on each atom are less than 0.01 eV/Å.

4. Results and discussion

4.1. Structural characterization

In order to investigate the effect of defect state modulation of ZnO by interaction of different types of ions, we have synthesized bare, cation doped and anion-attached ZnO NP samples. Fig. 1a shows XRD patterns of native ZnO (black) and Mn-ZnO (red). XRD patterns of Mn-doped ZnO are similar to that of native ZnO and consistent with the diffraction pattern of pristine bulk ZnO wurtzite structure as available in the literature [26]. Fig. 1b depicts the morphology of the as-synthesized ZnO and Mn-doped ZnO (inset) obtained from FESEM, which indicates no significant change in grain size. The chemical composition of the Mn-doped ZnO was confirmed by EDAX analysis as shown in Fig. 1c.From the EDAX measurement, it is observed that 2.3 wt% of Mn^{2+} is doped into the ZnO crystal lattice. Elemental mapping further confirms the elemental homogeneity of Zn, O and Mn atoms in the Mn-doped ZnO system as evident from Fig. 1d. The high resolution transmission electron microscope images of synthesized ZnO and Mn-doped ZnO sample confirmed the crystallinity of lattice. Fig. 1e and 1f shows the HRTEM image of ZnO and Mn-doped ZnO (5 nm), whereas Fig. 1g and 1h shows the same for 30 nm NPs. The fringe width for 5 nm ZnO and Mn-doped ZnO NPs are 0.264 and 0.262 nm respectively, which corresponds to the spacing between (002) planes [27,28]. The fringe width for 30 nm ZnO and Mn-doped ZnO NPs are 0.278 and 0.286 nm respectively, corresponding to the spacing between (100) planes [28].

4.2. Optical characterization

To explore the optical properties, the steady state absorption and emission spectra of the ZnO, Mn-doped ZnO and Cl-attached ZnO (5 nm NPs) were obtained. Fig. 2a shows the UV–vis absorption spectra of ZnO (black) indicating peaks at 336 nm, which get shifted to 326 nm for Mn-doped system (red in color). There is no clear peak shift in case of Cl-attached ZnO (inset).The shift of absorption edge towards blue end of spectra by Mn doping suggests an increment in the band gap due to increased population of all the states close to conduction band as a result of doping [29,30]. The significant change in absorption spectra suggests a substitutional doping of Mn^{2+} in crystal lattice [31] while chloride ions are expected to get attached at the surface.

The room temperature PL spectrum of ZnO NP is comprised of two emission bands upon excitation above the band-edge (λ_{ex} = 336 nm) as shown in Fig. 2b. The narrow UV band centered at 377 nm in the emission spectra of ZnO NPs is due to the band gap emission. The broad emission near the blue green region with a peak at 530 nm is due to defect centers located near the surface. The broad emission is composed of two bands: one arises from the doubly charged vacancy center V_0^{++} located at 555 nm (P_2) and the other arises from the singly charged vacancy center V_0^{+} located at 500 nm (P_1) [32,33].The emission intensity of Mn-doped ZnO NPs decreases considerably than ZnO as presence of dopant Mn^{2+} ion increases defect states. These may provide competitive pathway for electron-hole recombination [34]. As supported by our first principles calculation for ZnO nanocluster, there is a significant increase in oxygen-vacancy formation energy in presence of Mn dopant. Inset of Fig. 2b shows band-gap emission after Mn-doping. Cl-attached ZnO NPs shows lesser green luminescence as shown in Fig. 2c. The intensity of the green luminescence is decreased with the increment of Cl concentration in the aqueous solution. As seen in theoretical calculations, surface attachment of chloride ions reduce the oxygen vacancy states, which was also experimentally observed in reference [35]. In addition, introduction of some new non-radiative relaxation pathways can reduce visible luminescence [36]. The fluorescence decay profile of the ZnO NPs in the presence and absence of dopant ion was obtained upon excitation with 375 nm laser and monitored at 530 nm (Fig. 3a). The excited state lifetime of the ZnO NPs quenches for both the cases of Mn^{2+} doping or chloride ion attachment. The details of the spectroscopic parameters and the fitting parameters of the fluorescence decays are tabulated in Table 1. The decrease in average life time of Mn-doped ZnO NPs and Cl-attached ZnO NPs can be attributed to a significant electronic interaction [34] between ZnO and the corresponding attached ions. Presence of an additional faster component of 0.3 ns for both Cl-attached ZnO and Mn-doped ZnO contributes nearly 50% of their decay profiles. It indicates that there is a significant charge transfer process involved between ZnO and those ions. The electronic cross-talking indeed proves the

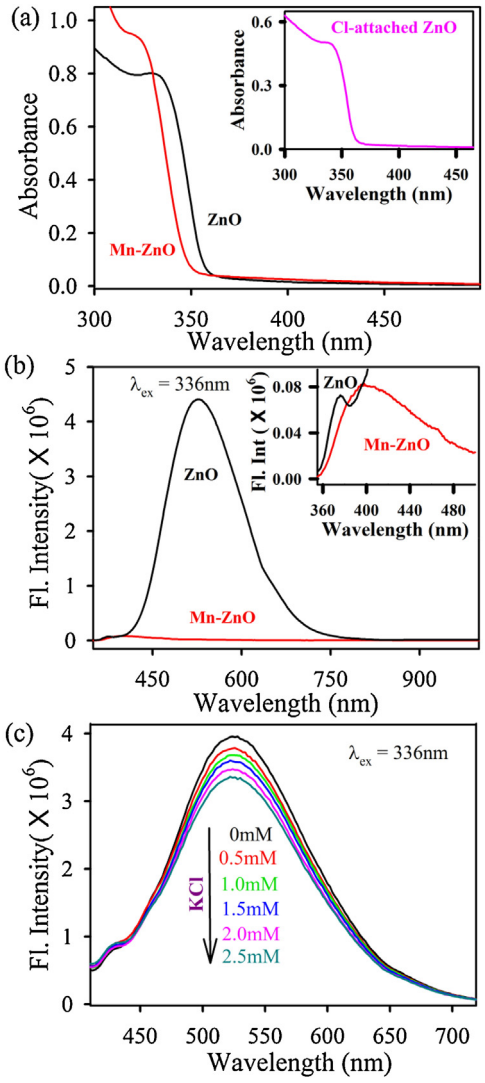

Fig. 2. (a) Absorption spectra of ZnO (black), Mn-doped ZnO (red). Inset shows the absorption spectra of chloride attached ZnO. (b) Emission spectra of ZnO and Mn-doped ZnO (red) indicate a significant decrease in intensity after doping. Inset shows band gap emission spectra of the same samples. The excitation wavelength is 336 nm. (c) Depicts the change in emission spectra of ZnO by addition of increasing concentration of KCl. The excitation wavelength is 336 nm. (For interpretation of the references to color in this figure legend, the reader is referred to the web version of this article.)

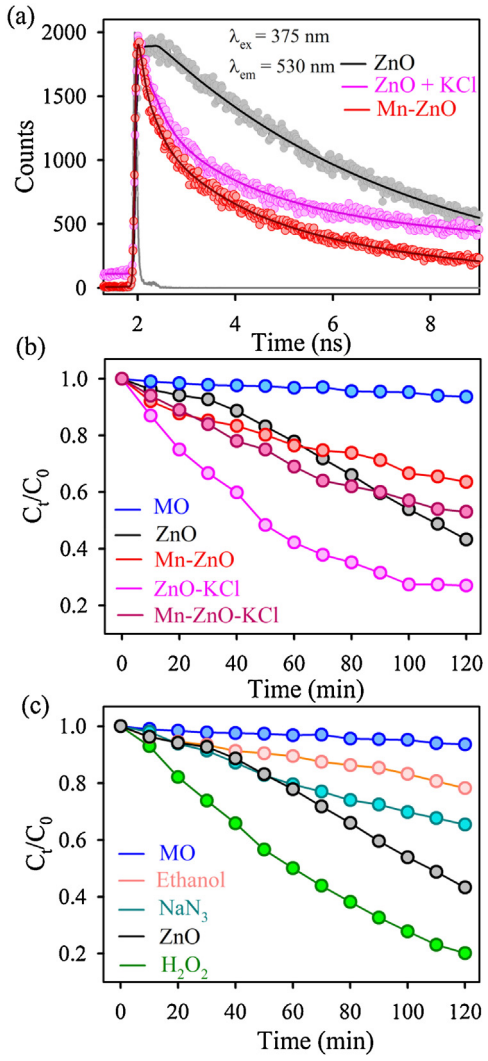

Fig. 3. (a) The picosecond-resolved fluorescence transients of ZnO (black), chloride attached ZnO (pink) Mn-doped ZnO (red). The excitation wavelength is 375 nm and the decay profile was collected at 530 nm. (b) Photocatalytic degradation of MO in the presence of ZnO (black), Mn-doped ZnO (red) Cl attached ZnO (pink) and Cl attached Mn-doped ZnO (dark red) under UV light irradiation. (c) Photocatalytic degradation of MO by ZnO (black) and in presence of sodium azide (cyan), ethanol (fade red) and H_2O_2 (green) under UV light irradiation. (For interpretation of the references to color in this figure legend, the reader is referred to the web version of this article.)

Table 1
Excited state lifetimes of ZnO, Cl attached ZnO and Mn-doped ZnO.

System	τ_1 (ns)	τ_2 (ns)	τ_3 (ns)	τ_{avg} (ns)
ZnO	–	3.4(3%)	5.3(97%)	5.3
Cl-attached ZnO	0.3 (41%)	1.9 (36%)	14.2 (23%)	4.1
Mn-doped ZnO	0.3 (53%)	3.4 (42%)	15.0 (5%)	2.4

The values in parentheses represent the relative weight percentages of the time components. PL emissions were detected at 530 nm upon excitation at 375 nm.

successful interaction of ZnO either with dopant Mn^{2+} ions or with the surface attached chloride ions (Scheme 1).

4.3. Application in photocatalysis

In order to investigate the manifestation of the interfacial charge transfer dynamics in structurally modulated ZnO NPs, the photocatalytic activity has been studied using methyl orange (MO) as a model pollutant. Photocatalysis involves charge carrier generation from oxide based semiconductor nanomaterials and recognized as a green technology for the purification of water. 5 nm ZnO NP is not stable in water so we did the photocatalytic experiment in 30 nm ZnO NP. The photocatalytic activity of the Cl-attached ZnO NPs and Mn-doped ZnO NPs (of 30 nm NP) for degradation of MO under UV–vis was compared with ZnO NPs. Fig. 3b demonstrates the efficient photocatalytic activity of Cl-attached ZnO (~70%) in comparison to control ZnO (~55%) under 120 min UV–vis light irradiation ($\lambda \geq 365$ nm). However, Mn-ZnO NPs were used as a positive control to create more defects in the system. It is found that it exhibits much lower ~30% MO degradation in comparison to ZnO under similar illumination conditions. Upon attachment of chloride ion on Mn-doped ZnO the catalytic activity increased to ~45%. These observations suggest that due to efficient charge separation at the interface between Mn^{2+} and ZnO, the dopant impurities can generate large capture cross section for excitons, acting as trap states [37,38]. After attachment of the chloride ion, the trap states are partially healed resulting higher photocatalytic activity. However, during photocatalytic reaction, photoinduced electrons and holes escape recombination when it consist of large amount of chloride ions at the surface which consequently generates (in the presence of oxygen and water) highly oxidative radicals ROS, that can degrade the organic pollutants. A large number of reactive species including h^+, OH^- are involved in the photocatalytic oxidation process. Hence, the effects of ROS scavengers and initiator on the degradation of MO were examined to elucidate the reaction mechanism. The effects of a scavenger (sodium azide) and initiator (H_2O_2) on the degradation efficiency of MO are shown in Fig. 3c. The degradation efficiency of ZnO for MO is reduced to 35% after adding sodium azide, whereas it increased to 80% in presence of H_2O_2. These observations clearly suggest that the photocatalytic degradation proceed via ROS mechanism [39].

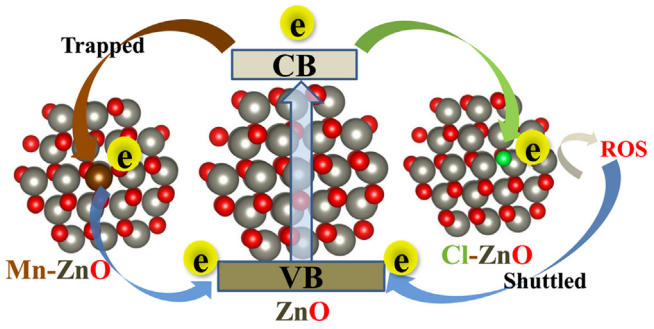

Scheme 1. Schematic representation of various electron shuttling pathways in structurally modulated ZnO nanostructure leading to dissimilar photocatalytic activity.

4.4. First principles computational investigation

4.4.1. ZnO nanocluster

To obtain an insight of catalytic activities of ZnO under Mn-doping and chloride assisted surface modification, we have investigated the electronic structure of ZnO-cluster under various experimentally probable situations. The atom (APDOS) and orbital projected (OPDOS) density of states for the optimized $Zn_{50}O_{50}$ cluster in pristine form and in presence of different types for oxygen vacancies are plotted in Fig. 4(a), (b) and (c), where we have investigated the impact of surface and core oxygen vacancies. For bulk ZnO, where Zn^{2+} with valence configuration $3d^{10}4s^0$ is in tetrahedral coordination with O^{2-} ligands ($2s^2 2p^6$), there is a band-

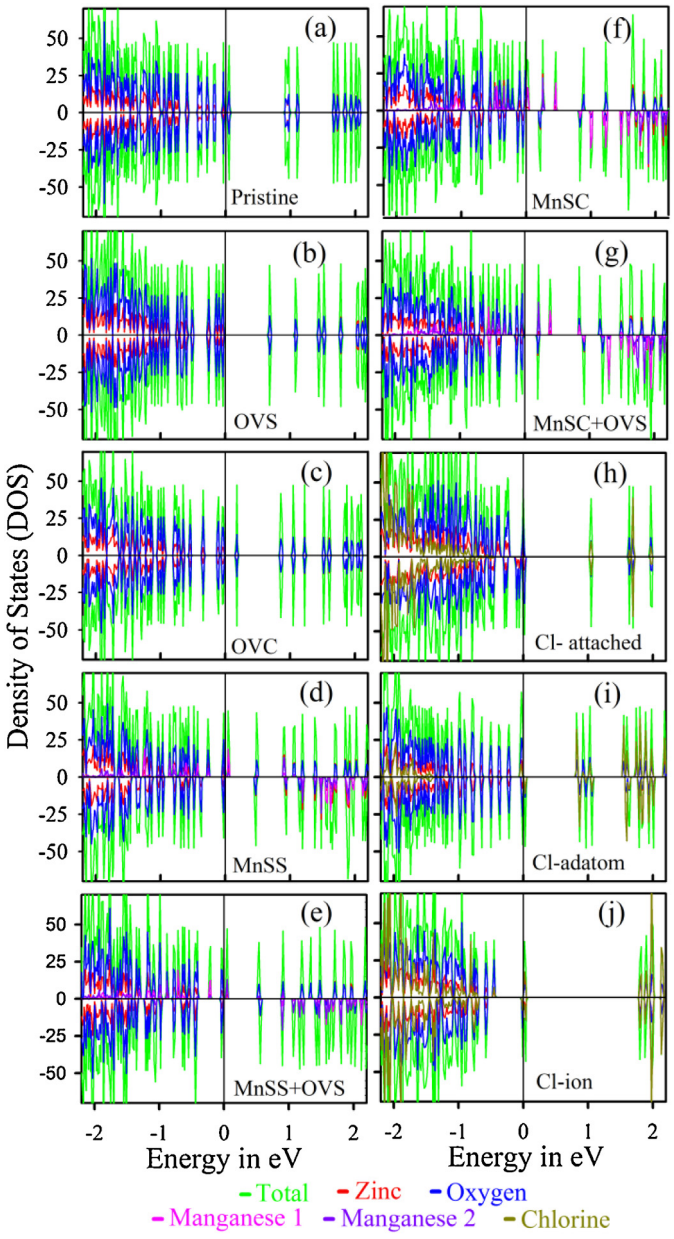

Fig. 4. Atom (APDOS) and orbital projected (OPDOS) density of states of (a) ZnO Nanocluster, (b) ZnO Nanocluster with oxygen vacancy on surface (OVS) and (c) ZnO Nanocluster with oxygen vacancy in core (OVC). Mn-doped ZnO (d) both of the Mn is on surface (MnSS), (e) both of the Mn is on surface with a nearest neighbour oxygen vacancy on surface (MnSS + OVS), (f) one Mn is on surface and another one is in core (MnSC) and (g) one Mn is on surface and another one is in core with a nearest neighbour oxygen vacancy on surface (MnSC + OVS). (h) Cl-attached ZnO Nanocluster, (i) ZnO Nanocluster with oxygen vacancy on surface and a nearby Cl-adatom and (j) ZnO Nanocluster with oxygen vacancy on surface and a nearby Cl-ion. The DOS is plotted for all Zn-3*d* and all O-2*p* levels.

gap of ~3.3 eV. For $Zn_{50}O_{50}$ cluster, due to change of coordination near surface and surface reconstruction, there are shallow surface states near Fermi level (E_F), constituting of partially unfilled Zn-3*d* and O-2*p* levels of surface Zn and O atoms. There is a gap of ~0.8 eV in Fig. 4(a), which is well-known to be underestimated for density functional calculations. Nevertheless, a scaling of the theoretical value of band-gap to the experimentally obtained value (3.3 eV) may provide an approximate quantitative estimate of position of various orbital states. Additionally, qualitative comparison with all possible experimental situations also enables us to predict the presence of shallow levels and deep trap states in the system.

In Fig. 4(b) and (c), total and partial DOS are plotted for the same cluster in presence of single Oxygen vacancy at the surface (OVS) and at the core (OVC) respectively. In both of these cases, there is a shift of Fermi-level (E_F) towards conduction band, indicating an *n*-type doping. In addition, there are defect-induced deep trap states within band-gap, as can be seen from comparison of Fig. 4(a)–(c). In nano-sized systems, experimental probability of occurrence for OVS is much more than OVC. It may also be noted that the trap state generated in the case of OVS (Fig. 4b) are about 2.63 eV (considering scaling factor as described above) away from the valance band and very much consistent with the experimentally observed P_1 (2.5 eV from valance band) state in the NPs [33].

Fig. 5(a),(b) depict the charge density distribution of the pristine cluster and OVS cases. Surface charge redistribution in presence of OVS is evident from Fig. 5(b). The formation energies of oxygen vacancies for OVS and OVC are calculated to be 4.2 and 5.6 eV respectively, indicating the presence of OVS to be more energetically favourable.

4.4.2. Mn-doped ZnO

Next, the effects of Mn-doping in $Zn_{50}O_{50}$ cluster was investigated for four such experimentally probable situations, *viz.* (1) Two Mn (Mn1 and Mn2), substituting two nearest neighbour (*nn*) surface Zn atoms (MnSS); (2) MnSS with nearest neighbour surface oxygen vacancy (MnSS + OVS); (3) Two Mn substituting one Zn at core and one at surface (MnSC) and (4) MnSC with nearest neighbour surface oxygen vacancy (MnSC + OVS). Formation of MnSS system is energetically more favourable than the MnSC case both with and without OVS. For all these four cases, ferromagnetically aligned spin of the two Mn ions are lower in energy compared to antiferromagnetic alignment. The corresponding AP and OPDOS for ferromagnetic alignment are plotted in Fig. 4(d)–(g). The formation energies of a nearest neighbour OVS for all these four cases are ~ 14–15 eV, with the formation probability being more for MnSS case. However, comparison of formation energies for pristine system indicates that formation of OVS is less favourable for Mn-doped cluster.

The magnetic moments acquired by Mn1 and Mn2 are also higher for surface Mn atoms because of high surface reconstruction due to surface charge redistribution. Practically, the Mn-doped experimental system will be a combination of all the above four combinations. For MnSS cases, relative shift of E_F is towards conduction band, indicating an *n*-type charge transfer from Mn1 and Mn2 −3*d* levels to the *nn* surface Zn-3*d* and O-2*p* empty states. This charge transfer is evident from the highly hybridized Mn1 and Mn2-3*d*, Zn-3*d* and O-2*p* states in Fig. 4(d) and (e) and also from the corresponding charge-density plot in Fig. 5(c) and (d). On the contrary, there is a *p*-type doping and a reverse charge transfer from core Zn-3*d* filled states to the *nn* core Mn-3*d* levels for MnSC cases, as can be seen from Fig. 4(f) and (g). An important outcome of Mn-doping within $Zn_{50}O_{50}$ cluster is the appearance of many deep defect-induced trap-states within the band-gap for all the four cases (MnSS, MnSS + OVS, MnSC, MnSC + OVS), as can be seen from Fig. 4(d)–(g). These deep trap states capture the carriers and act as a recombination generation centers, rendering a reduction of photocatalytic activities, which has also been observed experimentally. The number and position of trap states are tabulated in Table 2. To simulate the carrier trapping, we have carried out a total energy comparison for MnSS and MnSC cases, after increasing the total number of electrons within the system. Increase in the number of electrons is observed to induce an increase in the total energy of the system, implying a loss of stability of the system with increased number of carriers. We may also mention in passing that in the current study, we are more interested to focus on the photocatalytic activities of Mn-doped systems and therefore have

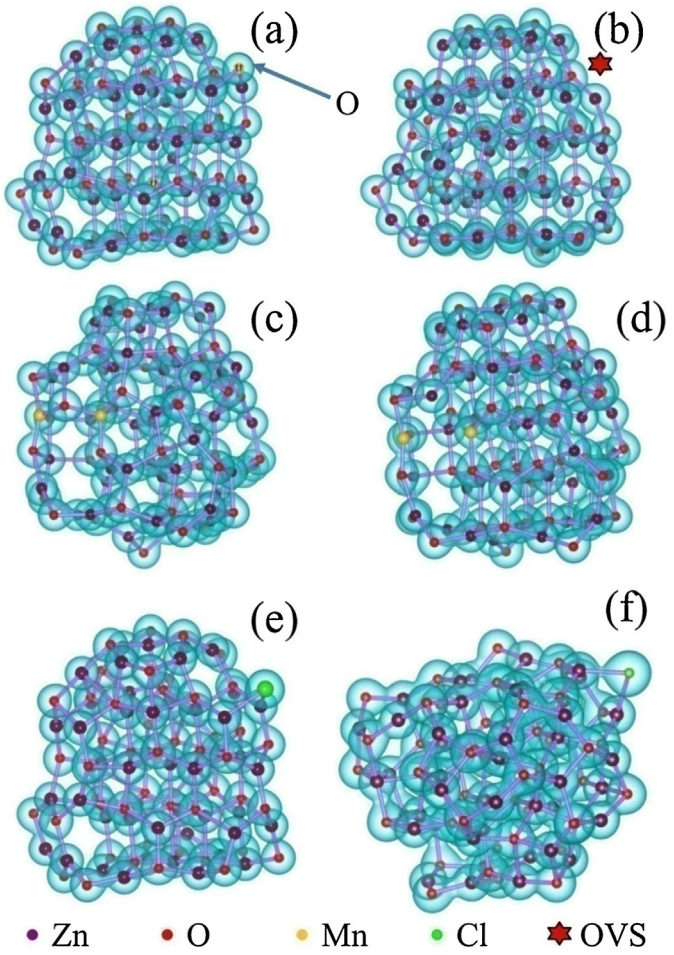

Fig. 5. Charge density plot of (a) ZnO Nanocluster, (b) ZnO Nanocluster with Oxygen vacancy on surface (c) MnSS (d) MnSS + OVS (e) ZnO Nanocluster with oxygen vacancy on surface and a nearby Cl-adatom and (f) ZnO Nanocluster with oxygen vacancy on surface and a nearby Cl-ion. Magenta and red indicate Zinc and Oxygen respectively. Yellow and green indicate Mn atoms and Cl atom respectively. Red star symbol stands for oxygen vacancy state at surface. (For interpretation of the references to color in this figure legend, the reader is referred to the web version of this article.)

Table 2
Number of trap state, position of trap state and nature of trap state of several configurations of ZnO, Mn-doped ZnO and chloride attached ZnO.

System	No of Trap State	Position of Trap state (eV)	Nature of trap state
ZnO pristine	–	Nil	Nil
ZnO + OVS	1	0.63	Surface Defect
ZnO + OVC	1	0.24	Surface Defect
MnSS	1	0.37	Deep
MnSS + OVS	1	0.41	Deep
MnSC	4	0.12, 0.16, 0.36, 0.72	Deep
MnSC + OVS	2	0.15, 0.35	Deep
Cl-attached	1	0.93	Deep
Cl-ad atom	0	Nil	Shallow acceptor
Cl-ion	0	Nil	Shallow acceptor

avoided the introduction of electron correlation explicitly (in terms of Hubbard U) for the narrow Mn-3*d* levels at E_F.

4.4.3. Chloride attached ZnO

To understand the increased photocatalytic activities for chloride attached systems, we have considered three situations, *viz*., (1) Cl-atom substituting an O-atom on the surface of $Zn_{50}O_{50}$cluster, (2) Cl-ad atom near an OVS on the same cluster, (3) Cl-ion near an OVS on the same cluster. All these three cases are seen to have introduced a *p*-type doping, where the E_F is shifting towards valence band. The corresponding AP and OPDOS are plotted in Fig. 4(h)-(j). The extent of *p*-type doping is highest for the third case. For case (1), there is very little charge transfer from surface Zn-3*d* and O-2*p* to Cl-3*p*, as can be seen from Fig. 4(h), which introduces very little magnetic moment (0.3 μ_B) within the system by partially filling the unfilled surface states of the pristine cluster due to surface reconstruction after geometrical optimization. For case (2) and (3), in presence of an OVS, both the Cl ad atom and Cl^- ion settle at the OVS place and gets chemically bonded with the two *nn* Zn atoms. This implies that surface oxygen vacancies may be the favourable Cl-doping sites within the cluster. In these two cases, shallow Cl-3*p* induced acceptor levels are generated very near to the valence band (within ~0.1 eV). These acceptor levels are also highly hybridized with Zn-3*d* and O-2*p* levels, indicating a partial charge transfer from those levels to Cl-3*p*. Surface charge redistribution will be also evident from the charge-density plots as presented in Fig. 5(e) and (f) for cases (2) and (3) respectively. Due to higher amount of charge transfer, for case (3), the attached cluster has acquired a higher total magnetic moment (0.8 μ_B) than case (2) (0.5 μ_B). Among these three situations, the third one is also the lowest in total energy. Presence of shallow acceptor levels and absence of deep trap-states for Cl-attached systems may be the root cause behind the halide assisted increase of photocatalysis. All these three cases, in contrary to the Mn-doped system, acquire better stability with increase of the total number of electrons within the system.

5. Conclusion

In the present work, it is shown that defect state modulation of wide band-gap semiconductor ZnO using halide atom namely chloride ion can modify its photocatalytic activity significantly. ZnO NPs, chloride attached ZnO NPs and Mn-doped ZnO NPs (of size around 5 nm and 25–30 nm) have successfully synthesized and structurally characterized using SEM, TEM and XRD. The optical absorption shows a clear indication of Mn^{2+} doping within bulk, while Cl^- is attached to the surface states. The photocatalytic activity of structurally modulated ZnO NPs, has been studied using methyl orange (MO) as a model pollutant. For Cl-attached ZnO, chloride ion at the surface of ZnO can shuttle the photo-excited electrons to the surface, resulting in an increased ROS generation and higher photocatalytic activity. On the contrary, dopant atom Mn^{2+} can act as a trapping site for the excitons and consequently reduce the activity. Upon addition of chloride ion, trap states of Mn-doped ZnO can also be healed resulting in higher photo-catalytic activity. The results suggested that tuning of defect states in semiconductor nanostructures can be extremely beneficial for diverse photocatalytic activities.

Acknowledgments

T.K.M. and D. B. wishes to acknowledge the support of DST India for INSPIRE Research Fellowship for funding. P.K. thanks Council of Scientific and Industrial Research (CSIR India) for fellowship. We thank the Department of Science and Technology (DST, India) for financial grant SB/S1/PC-011/2013. We also thank DAE (India) for financial grant 2013/37P/73/BRNS. DK would like to acknowledge BARC ANUPAM supercomputing facility for computational resources.

References

[1] D. Bernti, Water pollution: a problem with global dimensions, Ambio 3 (1974) 139–145.
[2] R.P. Schwarzenbach, T. Egli, T.B. Hofstetter, U. Von Gunten, B. Wehrli, Global water pollution and human health, Annu. Rev. Environ. Resour. 35 (2010) 109–136.
[3] A. Sugunan, J. Dutta, Pollution treatment, remediation and sensing, Nanotechnology 2 (2010) 125–147.
[4] A.O. Ibhadon, P. Fitzpatrick, Heterogeneous photocatalysis: recent advances and applications, Catalysts 3 (2013) 189–218.
[5] M.R. Hoffmann, S.T. Martin, W. Choi, D.W. Bahnemann, Environmental applications of semiconductor photocatalysis, Chem. Rev. 95 (1995) 69–96.
[6] A. Fujishima, K. Honda, Electrochemical photolysis of water at a semiconductor electrode, Nature 238 (1972) 37–38.
[7] S. Hernández, D. Hidalgo, A. Sacco, A. Chiodoni, A. Lamberti, V. Cauda, E. Tresso, G. Saracco, Comparison of photocatalytic and transport properties of TiO2 and ZnO nanostructures for solar-driven water splitting, Phys. Chem. Chem. Phys. 17 (2015) 7775–7786.
[8] Y. Li, W. Xie, X. Hu, G. Shen, X. Zhou, Y. Xiang, X. Zhao, P. Fang, Comparison of dye photodegradation and its coupling with light-to-electricity conversion over TiO2 and ZnO, Langmuir 26 (2009) 591–597.
[9] Y. Guo, X. Cao, X. Lan, C. Zhao, X. Xue, Y. Song, Solution-based doping of manganese into colloidal ZnO nanorods, J. Phys. Chem. C 112 (2008) 8832–8838.
[10] S. Sarkar, A. Makhal, S. Baruah, M.A. Mahmood, J. Dutta, S.K. Pal, Nanoparticle-sensitized photodegradation of bilirubin and potential therapeutic application, J. Phys. Chem. C 116 (2012) 9608–9615.
[11] S. Baruah, S.K. Pal, J. Dutta, Nanostructured zinc oxide for water treatment, J. Nanosci. Nanotechnol.-Asia 2 (2012) 90–102.
[12] Y. Chergui, D. Mekki, N. Nehaoua, Comparative Study of Dye-Sensitized Solar Cell Based on ZnO and TiO2 Nanostructures, INTECH Open Access Publisher, 2011.
[13] A. Kohan, G. Ceder, D. Morgan, C.G. Van de Walle, First-principles study of native point defects in ZnO, Phys. Rev. B 61 (2000) 15019.
[14] D. Chen, Z. Wang, T. Ren, H. Ding, W. Yao, R. Zong, Y. Zhu, Influence of defects on the photocatalytic activity of ZnO, J. Phys. Chem. C 118 (2014) 15300–15307.
[15] M.Y. Guo, A.M.C. Ng, F. Liu, A.B. Djurisic, W.K. Chan, H. Su, K.S. Wong, Effect of native defects on photocatalytic properties of ZnO, J. Phys. Chem. C 115 (2011) 11095–11101.
[16] V. Roy, A. Djurišić, H. Liu, X. Zhang, Y. Leung, M. Xie, J. Gao, H. Lui, C. Surya, Magnetic properties of Mn doped ZnO tetrapod structures, Appl. Phys. Lett. 84 (2004) 756–758.
[17] G. Shen, J.H. Cho, J.K. Yoo, G.-C. Yi, C.J. Lee, Synthesis and optical properties of S-doped ZnO nanostructures: nanonails and nanowires, J. Phys. Chem. B 109 (2005) 5491–5496.
[18] J. Wang, Z. Wang, B. Huang, Y. Ma, Y. Liu, X. Qin, X. Zhang, Y. Dai, Oxygen vacancy induced band-gap narrowing and enhanced visible light photocatalytic activity of ZnO, ACS Appl. Mater. Interfaces 4 (2012) 4024–4030.
[19] S. Sardar, P. Kar, S. Sarkar, P. Lemmens, S. Pal, Interfacial carrier dynamics in PbS-ZnO light harvesting assemblies and their potential implication in photovoltaic/photocatalysis application, Sol. Energ. Mat. Sol. 134 (2015) 400–406.
[20] R. Hong, J. Li, L. Chen, D. Liu, H. Li, Y. Zheng, J. Ding, Synthesis, surface modification and photocatalytic property of ZnO nanoparticles, Powder Technol. 189 (2009) 426–432.
[21] S. Sardar, P. Kar, H. Remita, B. Liu, P. Lemmens, S.K. Pal, S. Ghosh, Enhanced charge separation and FRET at heterojunctions between semiconductor nanoparticles and conducting polymer nanofibers for efficient solar light harvesting, Sci. Rep. 5 (2015) 17313.
[22] D. Bagchi, S. Chaudhuri, S. Sardar, S. Choudhury, N. Polley, P. Lemmens, S.K. Pal, Modulation of stability and functionality of a phyto-antioxidant by weakly interacting metal ions: curcumin in aqueous solution, RSC Adv. 5 (2015) 102516–102524.
[23] P. Kar, S. Sardar, E. Alarousu, J. Sun, Z.S. Seddigi, S.A. Ahmed, E.Y. Danish, O.F. Mohammed, S.K. Pal, Impact of metal ions in porphyrin-based applied materials for visible-light photocatalysis: key information from ultrafast electronic spectroscopy, Chem. Eur. J. 20 (2014) 10475–10483.
[24] G. Kresse, J. Hafner, Ab initio molecular dynamics for liquid metals, Phys. Rev. B 47 (1993) 558.
[25] S. Grimme, Semiempirical GGA-type density functional constructed with a long-range dispersion correction, J. Comput. Chem. 27 (2006) 1787–1799.
[26] S.S. Kumar, P. Venkateswarlu, V.R. Rao, G.N. Rao, Synthesis, characterization and optical properties of zinc oxide nanoparticles, Int. Nano Lett. 3 (2013) 1–6.
[27] M. Alias, R. Aljarrah, H. Al-Lamy, K. Adem, Investigation the effect of thickness on the structural and optical properties of nano ZnO films prepared by dc magnetron sputtering, Int. J. Appl. Innov. Eng. Manag. (IJAIEM) 2 (2013) 198–203.
[28] A. Bagabas, A. Alshammari, M.F. Aboud, H. Kosslick, Room-temperature synthesis of zinc oxide nanoparticles in different media and their application in cyanide photodegradation, Nanoscale Res. Lett. 8 (2013) 1–10.
[29] E. Burstein, Anomalous optical absorption limit in InSb, Phys. Rev. 93 (1954) 632–633.
[30] T. Moss, The interpretation of the properties of indium antimonide, Proc. Phys. Soc. London Sect. B 67 (1954) 775–782.
[31] T.L. Tan, C.W. Lai, S.B. Abd Hamid, Tunable band gap energy of Mn-doped ZnO nanoparticles using the coprecipitation technique, J. Nanomater. 2014 (2014) 1–6.
[32] S. Sardar, S. Chaudhuri, P. Kar, S. Sarkar, P. Lemmens, S.K. Pal, Direct observation of key photoinduced dynamics in a potential nano-delivery vehicle of cancer drugs, Phys. Chem. Chem. Phys. 17 (2015) 166–177.
[33] A. Makhal, S. Sarkar, T. Bora, J. Dutta, A.K. Raychaudhuri, S.K. Pal, Dynamics of light harvesting in ZnO nanoparticles, Nanotechnology 21 (2010) 265703.
[34] Y.-H. Lu, W.-H. Lin, C.-Y. Yang, Y.-H. Chiu, Y.-C. Pu, M.-H. Lee, Y.-C. Tseng, Y.-J. Hsu, A facile green antisolvent approach to Cu 2+-doped ZnO nanocrystals with visible-light-responsive photoactivities, Nanoscale 6 (2014) 8796–8803.
[35] Y.-J. Choi, K.-M. Kang, H.-S. Lee, H.-H. Park, Non-laminated growth of chlorine-doped zinc oxide films by atomic layer deposition at low temperatures, J. Mater. Chem. C 3 (2015) 8336–8343.
[36] Y. Gong, T. Andelman, G.F. Neumark, S. O'Brien, I.L. Kuskovsky, Origin of defect-related green emission from ZnO nanoparticles: effect of surface modification, Nanoscale Res. Lett. 2 (2007) 297–302.
[37] J. Han, P. Mantas, A. Senos, Defect chemistry and electrical characteristics of undoped and Mn-doped ZnO, J. Eur. Ceram. Soc. 22 (2002) 49–59.
[38] M.G. Nair, M. Nirmala, K. Rekha, A. Anukaliani, Structural optical, photo catalytic and antibacterial activity of ZnO and Co doped ZnO nanoparticles, Mater. Lett. 65 (2011) 1797–1800.
[39] S. Sarkar, A. Makhal, T. Bora, K. Lakhsman, A. Singha, J. Dutta, S.K. Pal, Hematoporphyrin–ZnO nanohybrids: twin applications in efficient visible-light photocatalysis and dye-sensitized solar cells, ACS Appl. Mater. Interfaces 4 (2012) 7027–7035.